

# Degrees of Freedom for Radiating Systems

Mats Gustafsson<sup>ID</sup>, *Senior Member, IEEE*

**Abstract**—Electromagnetic degrees of freedom are instrumental in antenna design, wireless communications, imaging, and scattering. A large number of degrees of freedom enhance control in antenna design, influencing radiation patterns and directivity, while in communication systems, it links to spatial channels for increased data rates, reliability, and resolution in imaging. The correlation between computed degrees of freedom and physical quantities is not fully understood, prompting a comparison between classical estimates, Weyl’s law, modal expansions, and optimization techniques. In this article, it is shown that the number of degrees of freedom for arbitrarily shaped radiating structures approaches the shadow area measured in squared wavelengths asymptotically as the wavelength decreases.

**Index Terms**—Antenna theory, capacity, computational electromagnetics, degrees of freedom, electromagnetic theory, inverse source problems, radiation modes.

## I. INTRODUCTION

ELECTROMAGNETIC degrees of freedom (DoF) find importance across a wide range of electromagnetic (EM) applications, spanning antenna design, wireless communication systems, scattering problems, and measurement techniques [1], [2], [3], [4], [5], [6], [7], [8], [9], [10], [11]. The number of DoF (NDoF) emerges as a crucial factor in achieving desired performance levels. For instance, in antenna design, higher NDoF facilitate enhanced control over radiation patterns and maximum directivity [6]. In wireless communication systems, NDoF correlate with the number of channels or spatial dimensions utilized for signal transmission, thereby providing higher data rates and improved reliability, especially in technologies like multiple-input-multiple-output (MIMO) systems and intelligent surfaces [7], [9].

The relationship between the NDoF and the electrical size of an object has been explored for at least half-a-century investigating resolution in imaging systems [12] and antenna systems [13]. Small electrical sizes exhibit few DoF, while large sizes display numerous DoF and hence, for example, potentially higher directivity and narrow beamwidth. Analytically solvable cases such as spherical regions with radius  $a$  offer a simple estimate of  $2(ka)^2$  DoF [2] based on the first  $L \approx ka$  spherical modes for wavenumber  $k = 2\pi/\lambda$ , wavelength  $\lambda$ , and two polarization DoF. The number of propagating waves in hollow rectangular waveguides [14] is also solvable with asymptotically  $2\pi A/\lambda^2$  DoF for a cross-sectional area  $A$ . These results are traced back to

H. Weyl more than a century ago, who studied the eigenvalue distribution of the Laplace and Helmholtz operators [15], [16]. Alternative estimates based on Nyquist ( $\lambda/2$ ) sampling resulting in  $8A/\lambda^2$  DoF have also been extensively used [2], [4], [5], [17], [18]. Moreover, communication systems have recently been investigated for different configurations [7], [9], with  $2\pi A/\lambda^2$  DoF for planar apertures. In this article, Weyl’s law [15], [16] and its connection to the NDoF are first explored. Beyond its mathematical significance in spectral theory, Weyl’s law is also fundamental in explaining the NDoF in thermal radiation [16]. However, its relevance to the NDoF in antenna and communication systems has been largely overlooked. Weyl’s law demonstrates that the NDoF for arbitrarily shaped bodies scales with the surface area, measured in squared wavelengths. These NDoF can be interpreted as the DoF in a communication system between the body and the surrounding region. Weyl’s law provides a unified framework that extends previous results on the asymptotic NDoF of canonical shapes, such as spheres [2] and planar rectangles [7], [9], to arbitrarily shaped regions.

In antenna systems, it is more common to focus on radiating systems, where the antenna transmits energy to the far-field. This article shows that the radiating NDoF approaches the total shadow area of the region, measured in squared wavelengths. For convex shapes, this result matches the NDoF derived from Weyl’s law, but it differs for more general shapes. The reduction in NDoF for nonconvex shapes can be attributed to the blockage of some regions, which limits their contribution to the radiated fields.

The NDoF for radiating systems is crucial in antenna and communication system design, as it determines the maximum number of radiating fields that can be achieved in a constrained design region. Furthermore, it is directly related to the maximum achievable average gain of an antenna system when its beam is steered across all possible directions. This establishes a connection to the Hannan limit, which was originally derived for infinite planar arrays [19], [20]. Notably, this radiating NDoF is also twice the number of significant characteristic modes [10]. In communication systems, the derived asymptotic limit offers a straightforward estimate of the NDoF and thus the capacity [18]. This generalizes the results previously obtained for planar rectangular regions [7], [9] to arbitrarily shaped regions. The possibility of extending this framework to communication between arbitrarily shaped regions has also been explored [21].

The article is organized as follows. Section II introduces Weyl’s law and its applications for determining NDoF. Section III explores the concept of capacity and its connection to radiation modes and NDoF. In Section IV, the asymptotic

Received 8 April 2024; revised 28 November 2024; accepted 28 December 2024. Date of publication 7 January 2025; date of current version 5 February 2025. This work was supported by the Excellence Center at Linköping-Lund in Information Technology (ELLIIT) and the TICRA Foundation.

The author is with the Department of Electrical and Information Technology, Lund University, 22100 Lund, Sweden (e-mail: mats.gustafsson@eit.lth.se).

Digital Object Identifier 10.1109/TAP.2024.3524437

NDoF is analyzed in relation to the shadow area of a region. Electric and magnetic currents are examined in Section V. The NDoF in inverse problems is discussed in Section VI. Finally, the article is concluded in Section VII.

## II. WEYL'S LAW AND PROPAGATING MODES

The NDoF is most straightforwardly determined by the number of propagating modes in a waveguide. Canonical shapes such as rectangular or circular cross sections can be solved analytically [14]. These arbitrarily shaped cross sections can also be treated as a special case of Weyl's law [15], [16]. Weyl's law describes the distributions of eigenvalues  $v_n$  for the Laplace operator  $-\nabla^2 u_n = v_n u_n$  in a region  $\Omega \subset \mathbb{R}^d$  with Dirichlet or Neumann boundary conditions. The number of eigenvalues  $N_{Wd}(v)$  below  $v$  is asymptotically [15], [16]

$$N_{Wd}(v) = \frac{w_d |\Omega| v^{d/2}}{(2\pi)^d} \quad \text{as } v \rightarrow \infty \quad (1)$$

for a region  $\Omega$  with a volume  $|\Omega|$  (in  $\mathbb{R}^3$  or area in  $\mathbb{R}^2$  or length in  $\mathbb{R}^1$ ), with  $w_d = \pi^{d/2}/(d/2)!$  denoting the volume of the unit ball in  $\mathbb{R}^d$ . Weyl's law is also applicable to the number of positive eigenvalues for the Helmholtz equation in  $\Omega$

$$\nabla^2 u_n + k^2 u_n = \mu_n u_n \Leftrightarrow -\nabla^2 u_n = (k^2 - \mu_n) u_n \quad (2)$$

for a wavenumber  $k = 2\pi/\lambda$  with a wavelength  $\lambda$ . The number of propagating  $k^2 > \mu$  (scalar) modes in arbitrarily shaped waveguides is hence asymptotically

$$N_{Wd}(k^2) = \frac{w_d |\Omega| k^d}{(2\pi)^d} = \frac{w_d |\Omega|}{\lambda^d} \quad (3)$$

which reduces to

$$N_{W1} = \frac{k\ell}{\pi} = \frac{2\ell}{\lambda} \quad \text{and} \quad N_{W2} = \frac{k^2 A}{4\pi} = \frac{\pi A}{\lambda^2} \quad (4)$$

for a line with length  $\ell = |\Omega|$  in  $\mathbb{R}$  and an aperture surface with area  $A = |\Omega|$  in  $\mathbb{R}^2$  (see Fig. 1). Here, we note that the 1-D case corresponds to Nyquist ( $\lambda/2$ ) sampling. The 2-D case differs from Nyquist sampling in two orthogonal directions, even for the special case of a rectangular region [7], [14]. Explicit evaluation of a rectangular cross section provides a simple interpretation of the difference between  $\lambda/2$  for lines and the area scaling (4) for surfaces. Waves in 1-D start to propagate for sizes above half-a-wavelength. For a rectangular waveguide, propagating modes depend on the squared magnitude of oscillations in two transverse directions corresponding to the area of an ellipse or circle [14]. This difference is quantified by the unit ball  $w_d$  in Weyl's law (3), that is,  $w_1^2 = 4$  and  $w_2 = \pi$ .

These estimates (4) of the asymptotic number of propagating modes for (scalar) Helmholtz equation are doubled for Maxwell's equations when two orthogonal polarizations contribute

$$N_A = \frac{k^2 A}{2\pi} = \frac{2\pi A}{\lambda^2} \quad (5)$$

for an aperture with area  $A \in \mathbb{R}^2$ . The NDoF (5) is valid for arbitrarily shaped cross sections in the electrically large limit  $k \rightarrow \infty$ .

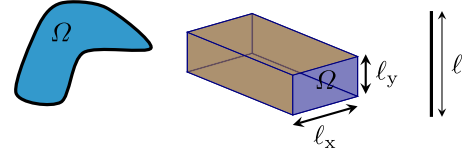


Fig. 1. Number of eigenvalues for Laplace and Helmholtz operators in a region  $\Omega$  is described by Weyl's law as applied to waveguides and line elements in (4).

Weyl's law (5) estimates the number of propagating modes in EM waveguide structures with perfect electric conductor (PEC) walls, but it is more challenging to apply Weyl's law for radiating structures in  $\mathbb{R}^3$ . Starting with a spherical region with radius  $a$  which is analytically solvable by expanding the radiated field in spherical waves [22], [23]. In contrast to waveguides, there is no clear cut-off between propagating and evanescent waves. There are  $2L(L+2)$  spherical modes up to order  $L$ , and modes of order  $L \geq ka$  become increasingly reactive [22]. Using the surface area of the sphere together with  $L \approx ka$  corresponds to approximately [2]

$$2(ka)^2 = \frac{k^2 A}{2\pi} = \frac{2\pi A}{\lambda^2} \quad (6)$$

propagating modes for  $ka \gg 1$  similar to the estimate from Weyl's law (5) for an aperture in  $\mathbb{R}^2$ .

An explanation for the absence of a clear transition between propagating and evanescent modes in the context of a sphere arises from its expanding surface area as the radial distance increases. Consequently, there is a proportional rise in the number of propagating modes with radial distance. This stands in sharp contrast to waveguiding structures, where the cross-sectional area, and thus the NDoF, remains constant along the propagation direction. Hence, the approximation  $L \approx ka$  emerges as a useful descriptor for the shift from predominantly propagating to evanescent waves.

Although the cutoff  $L \approx ka$  provides a good simple approximation for the order of radiating spherical waves. Improved estimates for near-field measurements [24] and computational techniques [25] can be used for more precise estimates. An alternative interpretation of the cutoff is that high-order modes are associated with large current amplitudes and hence low efficiency for radiators of finite conductivity. This is related to the rapidly increasing reactive near field for high-order modes, that is, there are large field (and current) amplitudes that do not contribute efficiently to the radiated power. These fields are associated with high losses and stored energy for antennas. This imbalance between the amplitude of the modes can also be interpreted as a communication channel with a large dynamical range between the singular values of the channel matrix requiring a high SNR.

Evaluating the number of radiating spherical waves with efficiency above a given threshold, here 50%, produces an estimate of the NDoF. Fig. 2 depicts the number of such radiating modes [8] on a spherical shell with surface resistivity  $R_s = 10^{-p}\eta_0$  and spherical ball with resistivity  $k\rho_r = 10^{-p}\eta_0$  for  $p = 3, 5, 7$  with  $\eta_0$  denoting the impedance of free space. Note that copper has a surface resistivity of approximately  $R_s \approx 0.01 \Omega/\square$  around 1 GHz and a resistivity of

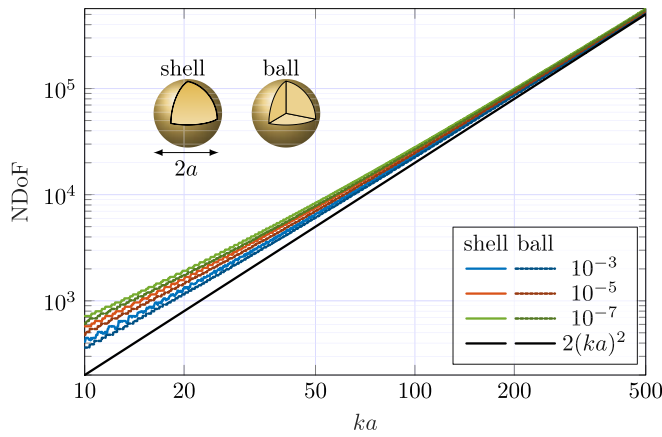


Fig. 2. NDoF from spherical modes with at least 50% efficiency for spherical shells with surface resistivity  $R_s = 10^{-p}\eta_0$  and balls with resistivity  $\rho_r = 10^{-p}\eta_0/k$  and both having radius  $a$  and  $p = 3, 5, 7$ . The NDoF is compared with the estimated  $2(ka)^2$  from (6).

$\rho_r \approx 10^{-8} \Omega \text{ m}$ . The results are compared with the estimate (6), and it is observed that the relative difference between the computed NDoF and  $2(ka)^2$  decreases as  $ka \rightarrow \infty$ . The radiation efficiencies for the spherical regions used in Fig. 2 are determined by expanding the current density and fields in spherical waves. The solution is expressed in radiation modes [26], [27] as given in Appendix A. Using material losses opens a possibility to generalize the NDoF to arbitrarily shaped radiators as analyzed in this article.

Arbitrarily shaped closed surfaces and disjoint regions are much more complex, for which it is also apparent that there are several alternative ways to interpret DoF, such as communication between regions [3], [11], [21], [28], from a region to a volume surrounding the region in Fig. 3(a), and from a region to the far-field in Fig. 3(b). In this article, we consider the radiating NDoF interpreted as the NDoF from a region to the far-field.

For arbitrarily shaped regions with smooth boundaries, we can interpret Weyl's law locally, resulting in an NDoF according to (5) with surface area  $A$ . However, these DoF will generally only propagate to the volume outside  $\Omega$  and not to the far-field. Instead, the NDoF can be considered to propagate from the region  $\Omega$  to a slightly enlarged version of  $\Omega$  as illustrated in Fig. 3(a). This short distance is considered fixed and translates to infinity many wavelengths in the high-frequency limit. Also, note that the NDoF is unbounded if this distance is removed.

### III. CAPACITY LIMITS AND RADIATION MODES

Treating arbitrarily shaped (nonconvex or nonconnected) regions  $\Omega \in \mathbb{R}^3$ , we can formulate a communication problem between transmitters in the region  $\Omega$  to receivers in the far-field, or equivalently, on a circumscribing sphere, as shown in Fig. 3(b). Current density  $\mathbf{J}(\mathbf{r})$  in the transmitting region  $\Omega$  constitutes sources for the radiated field. These currents can be expanded in a sufficiently large number of basis functions, with expansion coefficients collected in a column matrix  $\mathbf{I}$  [29]. Similarly, the radiated field is expanded in

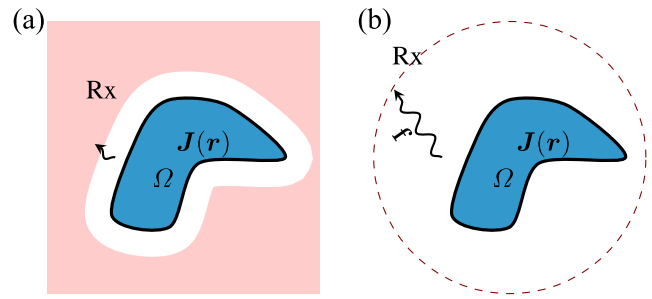


Fig. 3. DoF for a region  $\Omega \in \mathbb{R}^3$ . (a) Radiation to a volume surrounding  $\Omega$  related to Weyl's law (5). (b) Radiation to the far-field or a circumscribing sphere.

spherical waves [22], [23], with expansion coefficients collected in a column matrix  $\mathbf{f} = -\mathbf{U}\mathbf{I}$ , where  $\mathbf{U}$  denotes the projection of spherical waves onto the used basis functions [30]. The capacity (spectral efficiency) of this idealized system  $\mathbf{f} = -\mathbf{U}\mathbf{I} + \mathbf{n}$  is determined by [8]

$$\begin{aligned} & \text{maximize} && \log_2(\det(\mathbf{I} + \gamma \mathbf{U} \mathbf{P} \mathbf{U}^H)) \\ & \text{subject to} && \text{Tr}(\mathbf{R} \mathbf{P}) = 1 \\ & && \mathbf{P} \succeq \mathbf{0} \end{aligned} \quad (7)$$

where  $\mathbf{P} = \mathcal{E}\{\mathbf{I}\mathbf{I}^H\}$  denotes the covariance matrix of the currents,  $\mathbf{R}$  is the resistance matrix [29],  $\gamma$  quantifies the signal-to-noise ratio (SNR) from the additive noise  $\mathbf{n}$ , the superscript  $^H$  Hermitian transpose, and  $\mathbf{I}$  an identity matrix. In (7), the current is normalized to (two times) unit dissipated power [8]. To provide more realistic values for the capacity, physical properties can be considered. For antennas, it is common to incorporate limitations originating in the efficiency [8], [31] or bandwidth from the reactive energy around the antenna [31], [32].

The maximum capacity (7) is determined by water filling [33] for which it is convenient to rewrite (7) in a standard form by a change of variable  $\tilde{\mathbf{P}} = \mathbf{G} \mathbf{P} \mathbf{G}^H$ , where  $\mathbf{R} = \mathbf{G}^H \mathbf{G}$  is a factorization of the resistance matrix. Substituting into (7)

$$\begin{aligned} & \text{maximize} && \log_2(\det(\mathbf{I} + \gamma \mathbf{H} \tilde{\mathbf{P}} \mathbf{H}^H)) \\ & \text{subject to} && \text{Tr}(\tilde{\mathbf{P}}) = 1 \\ & && \tilde{\mathbf{P}} \succeq \mathbf{0} \end{aligned} \quad (8)$$

with the channel matrix  $\mathbf{H} = \mathbf{U} \mathbf{G}^{-1}$ . This problem is diagonalized by a singular value decomposition (SVD) of the channel matrix  $\mathbf{H}$ , that is, (square roots of the) eigenvalues of  $\mathbf{H}^H \mathbf{H} = \mathbf{G}^{-H} \mathbf{R}_0 \mathbf{G}^{-1}$ , which can be written  $\mathbf{G}^{-H} \mathbf{R}_0 \mathbf{G}^{-1} \mathbf{V}_n = v_n \mathbf{V}_n$ , where  $\mathbf{U}^H \mathbf{U} = \mathbf{R}_0$  is identified as the radiation matrix [27]. Simplifying by multiplication with  $\mathbf{G}^H$  and setting  $\mathbf{I}_n = \mathbf{G}^{-1} \mathbf{V}_n$  results in an eigenvalue problem for radiation mode efficiency

$$\mathbf{R}_0 \mathbf{I}_n = v_n \mathbf{R} \mathbf{I}_n = v_n (\mathbf{R}_0 + \mathbf{R}_\rho) \mathbf{I}_n. \quad (9)$$

The resistance matrix  $\mathbf{R} = \mathbf{R}_0 + \mathbf{R}_\rho$  is here decomposed into the radiation matrix  $\mathbf{R}_0 = \mathbf{U}^H \mathbf{U}$  modeling radiated power  $P_r = \mathbf{I}^H \mathbf{R}_0 \mathbf{I} / 2$  and the material matrix  $\mathbf{R}_\rho$  modeling Ohmic or dielectric losses  $P_\rho = \mathbf{I}^H \mathbf{R}_\rho \mathbf{I} / 2$ .

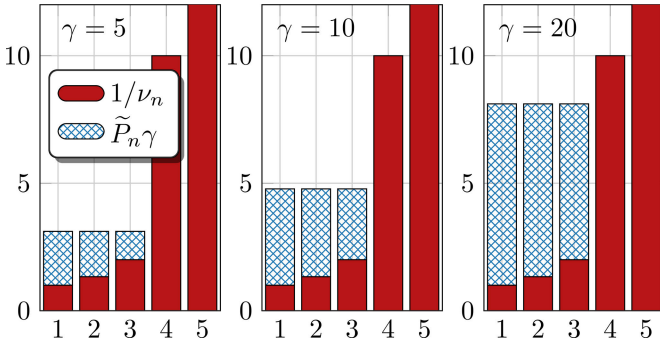


Fig. 4. Illustration of the water-filling solution (10) for radiation mode efficiencies  $\nu_n \in \{1, 0.75, 0.5, 0.1, 0.01\}$ . The red bars represent  $1/\nu_n$ , while the hashed blue bars indicate the allocated power  $\tilde{P}_n \gamma$  for the different modes.

Radiating modes diagonalizes (8), which solved using water-filling over radiation mode efficiencies  $\nu_n$  results in

$$\max_{\sum \tilde{P}_n=1} \sum_{n=1}^{\infty} \log_2(1 + \gamma \nu_n \tilde{P}_n) \quad (10)$$

with a finite number of nonzero power levels  $\tilde{P}_n \geq 0$  associated with radiation modes of sufficiently high efficiency. The number of used modes depends on the signal-to-noise ratio  $\gamma$  and the distribution of the modes  $\nu_n$ . Water-filling solutions for five efficiencies  $\nu_n \in \{1, 0.75, 0.5, 0.1, 0.01\}$  and SNRs  $\gamma \in \{5, 10, 20\}$  are depicted in Fig. 4. The reciprocals of the efficiencies,  $1/\nu_n$ , are large for inefficient modes, for example, mode 4 has  $1/\nu_4 = 10$ , and mode 5 has  $1/\nu_5 = 100$ . The normalized power level allocated to each mode,  $\tilde{P}_n \gamma$ , in the water-filling algorithm can be interpreted as determining the water level over a bottom profile defined by  $1/\nu_n$ , with a total amount of water  $\gamma = \sum \tilde{P}_n \gamma$ . The allocation of normalized power  $\tilde{P}_n \gamma$  and the number of active modes depends on the SNR,  $\gamma$ . For the low SNR,  $\gamma \ll 1$ , only the strongest mode, with  $1/\nu_1 = 1$ , contributes. As  $\gamma$  increases, power is quickly allocated to additional modes, such as modes 2 and 3, with  $1/\nu_2 \approx 1.33$  and  $1/\nu_3 = 2$ , respectively. Inefficient modes, such as  $1/\nu_4 = 10$ , require a significantly higher SNR to be activated, as shown in Fig. 4.

The capacity (10) is solely determined by the efficiencies  $\nu_n$  of the radiation modes and the SNR  $\gamma$ . Consequently, radiation modes can be regarded as fundamental physical quantities that quantify radiation properties and DoF for arbitrarily shaped objects with material losses [8].

Geometry and material properties are encapsulated within the radiation modes (9). To facilitate analysis, it is advantageous to distinguish between the radiation contribution  $\mathbf{R}_0$  and the material contribution  $\mathbf{R}_\rho$ . Radiation mode eigenvalues are defined by the generalized eigenvalue problem [26]

$$\mathbf{R}_0 \mathbf{I}_n = \varrho_n \mathbf{R}_\rho \mathbf{I}_n \quad (11)$$

with eigenvalues ordered decreasingly, that is,  $\varrho_n \geq \varrho_{n+1}$ , and efficiencies  $\nu_n = \varrho_n / (1 + \varrho_n)$  in (9). These modal currents are orthogonal over the material loss matrix  $\mathbf{I}_m^H \mathbf{R}_\rho \mathbf{I}_n = \delta_{mn}$  and radiated far fields  $\mathbf{f}_m^H \mathbf{f}_n = \mathbf{I}_m^H \mathbf{R}_0 \mathbf{I}_n = \varrho_n \delta_{mn}$ , where  $\delta_{mn}$  denotes the Kronecker delta. The number of radiation modes is infinite, but they diminish rapidly as  $\varrho_n \rightarrow 0$  for large

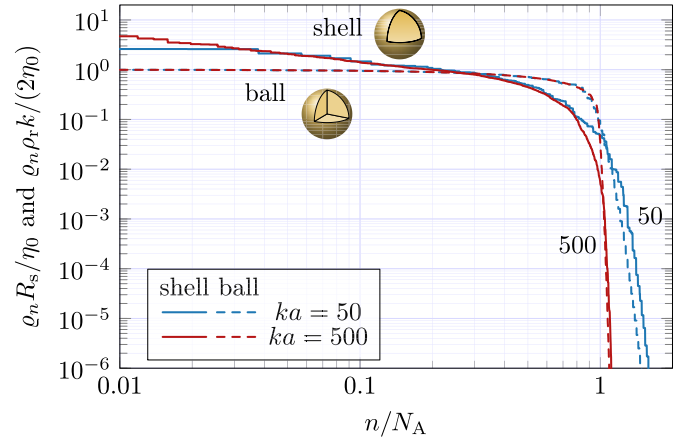


Fig. 5. Normalized radiation modes for spherical shells and spherical balls of the electrical sizes  $ka = 50$  and  $ka = 500$ . The mode index is normalized by the asymptotic NDoF  $N_A = 2(ka)^2$ .

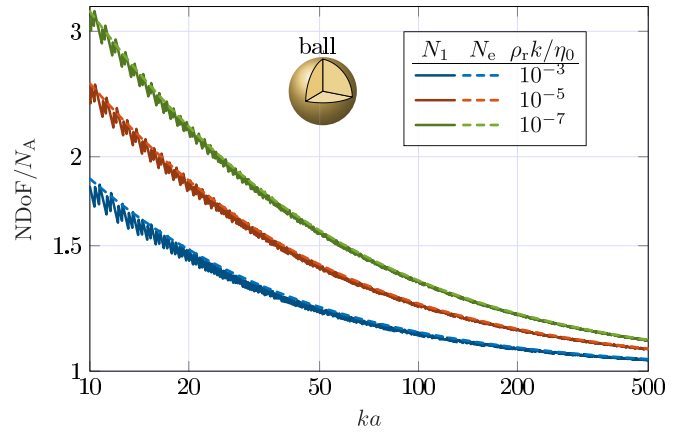


Fig. 6. Comparison between the NDoF  $N_1$  defined by 50% efficiency ( $\varrho_n \geq 1$ ) and the effective NDoF  $N_e$  in (13). The NDoFs are normalized by  $N_A = 2(ka)^2$  for spherical balls with resistivity  $\rho_r = 10^{-n} \eta_0 / k$  with  $n = 3, 5, 7$ .

$n$ , similar to the spherical waves in (6), to which they also reduce for spherical regions [27]. Radiation modes (11) are orthogonal and maximize the (Rayleigh) quotient between the radiated power and dissipated power in materials

$$\frac{\text{radiated power}}{\text{dissipated power in material}} = \frac{\mathbf{I}_m^H \mathbf{R}_0 \mathbf{I}_n}{\mathbf{I}_m^H \mathbf{R}_\rho \mathbf{I}_n} = \delta_{mn} \varrho_n \quad (12)$$

which can be used to define NDoFs from sufficiently efficient modes. Setting a threshold of 50% efficiency corresponding to radiation modes  $\varrho_n \geq 1$ , which is here used to define an NDoF  $N_1$  for arbitrarily shaped regions and material losses [8].

Fig. 5 depicts normalized radiation modes for spherical shells and spherical balls of the electrical sizes  $ka \in \{50, 500\}$  (see Appendix A). The spherical shell has surface resistivity  $R_s$ , and the spherical ball has resistivity  $\rho_r$ . Both the surface and volumetric objects exhibit similar normalized radiation modes, each showing a cutoff around  $n \approx N_A = 2(ka)^2$ . The cutoff becomes tighter with increasing electrical size, with the



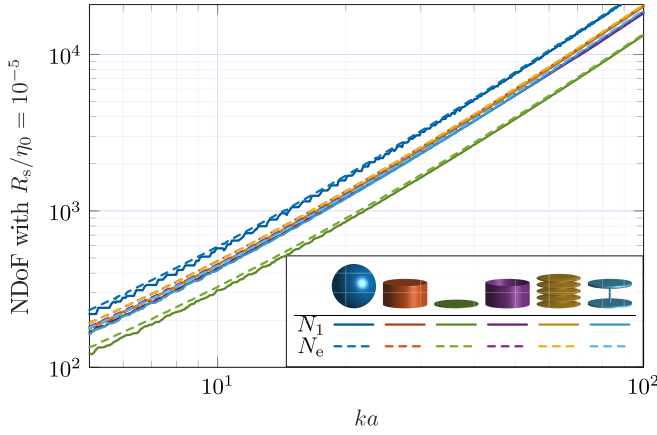


Fig. 7. NDoF  $N_1$  from radiation modes  $q_n \geq 1$  in (11) and  $N_e$  in (13) for the six objects in Table I with surface resistivity  $R_s = 10^{-5}\eta_0$ .

$ka = 500$  case approaching a step function for the spherical ball.

Alternatively, instead of using a threshold for efficiency, the effective NDoF [34], [35] can be utilized, which, when expressed in terms of radiation mode efficiency, is given by

$$N_e = \frac{(\text{Tr} \mathbf{H} \mathbf{H}^H)^2}{\|\mathbf{H} \mathbf{H}^H\|_F^2} = \frac{(\sum_{n=1}^{\infty} v_n)^2}{\sum_{n=1}^{\infty} v_n^2}. \quad (13)$$



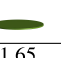



Fig. 6 compares the NDoF  $N_1$  based on 50% efficiency, as in Fig. 2, with the asymptotic effective NDoF  $N_e$  in (13). The depicted NDoFs are normalized with the estimate  $N_A = 2(ka)^2$  for the spherical region. The NDoF based on  $q_n \geq 1$  and the NDoF (13) agree well but the  $q_n \geq 1$  formulation oscillates due to the onset of modes at specific frequencies. The NDoFs for electrically smaller regions are above the  $N_A = 2(ka)^2$  estimate (6) but approaches it for larger sizes.

Radiation modes and hence NDoFs defined by (11) or (13) can be calculated for arbitrary shapes and material parameters. Fig. 7 shows an example of NDoFs for the six different shapes in Table I modeled by a surface resistivity  $R_s = 10^{-5}\eta_0$ . It is observed that the NDoF increases with the electrical size  $ka$ , with the spherical shell exhibiting the highest NDoF, followed by the solid cylinder and the corrugated cylinder, which have slightly higher NDoFs than the open cylinder and connected disks. The single disk exhibits the lowest NDoF. The effective NDoF (13) produces similar results but with fewer oscillations. This article demonstrates that the asymptotic number of NDoFs is proportional to the electrical size of the region's average shadow area  $\langle A_s \rangle$  in Table I (see also [10] for the corresponding number of significant characteristic modes).

#### IV. NDOFS AND SHADOW AREA

Determination of NDoFs from the number of radiation modes (11) greater than unity  $N_1$  or from the effective NDoF (13)  $N_e$  is easily achieved numerically for arbitrarily shaped objects and material parameters [8] (see Fig. 7). This numerical evaluation is complemented by an analytical examination, providing valuable physical insights and understanding. Specifically, it demonstrates that the radiating NDoF in the

TABLE I  
AVERAGE SHADOW AREA  $\langle A_s \rangle$ , SURFACE AREA  $A$ , AND HEIGHT-TO-RADIUS RATIO  $h/r$  FOR A SPHERE, CYLINDER, DISK, OPEN CYLINDER, CORRUGATED CYLINDER, AND CONNECTED DISKS. OBJECTS ARE CIRCUMSCRIBED BY A SPHERE WITH RADIUS  $a$

						
$\langle A_s \rangle / a^2$	3.14	2.53	1.65	2.21	2.45	2.19
$A / a^2$	12.6	10.1	6.59	10.3	21.9	11.3
$A / \langle A_s \rangle$	4.00	4.00	4.00	4.65	8.92	5.15
$h/r$	2.00	1.00	0.05	1.00	1.33	1.00

electrically large limit is proportional to the shadow area measured in squared wavelengths [10].

This proportionality can be derived using scattering or antenna theory. Here, employing antenna theory, the maximal effective area is first expressed in terms of radiation modes and subsequently related to the cross-sectional area of the object. The maximal partial effective area  $A_{\text{eff}} = \lambda^2 G / (4\pi)$ , and similarly the partial gain  $G$  in a direction  $\hat{\mathbf{k}}$  and polarization  $\hat{\mathbf{e}}$  are determined from the solution of [36]

$$\begin{aligned} &\text{maximize} \quad A_{\text{eff}} = \lambda^2 \mathbf{I}^H \mathbf{F}^H \mathbf{F} \mathbf{I} \\ &\text{subject to} \quad \mathbf{I}^H \mathbf{R} \mathbf{I} = 1 \end{aligned} \quad (14)$$

where  $\mathbf{F} \mathbf{I}$  is proportional to the  $\hat{\mathbf{e}}$ -component of the far-field in the direction  $\hat{\mathbf{k}}$ , and  $\mathbf{I}^H \mathbf{F}^H \mathbf{F} \mathbf{I}$  to the corresponding partial radiation intensity [36]. The solution of (14) is

$$\max A_{\text{eff}}(\hat{\mathbf{k}}, \hat{\mathbf{e}}) = \lambda^2 \mathbf{F}^H \mathbf{R}^{-1} \mathbf{F} \quad (15)$$

and taking the average of  $\max A_{\text{eff}}(\hat{\mathbf{k}}, \hat{\mathbf{e}})$  over all directions  $\hat{\mathbf{k}}$  and polarizations  $\hat{\mathbf{e}}$

$$\langle \max A_{\text{eff}} \rangle = \frac{1}{8\pi^2} \int_{2\pi} \int_{4\pi} \max A_{\text{eff}}(\hat{\mathbf{k}}, \hat{\mathbf{e}}) d\Omega_{\hat{\mathbf{k}}} d\Omega_{\hat{\mathbf{e}}} \quad (16)$$

and similarly for the average maximal partial gain  $\langle \max G \rangle = 4\pi \langle \max A_{\text{eff}} \rangle / \lambda^2$ . By diagonalizing the optimization problem (14) using the radiation modes (11) and performing the directional and polarization averaging (16) detailed in Appendix B, we derive a straightforward expression for the average maximal effective area, formulated in terms of the radiation modes

$$\langle \max A_{\text{eff}} \rangle = \frac{\lambda^2}{8\pi} \sum_{n=1}^{\infty} v_n = \frac{\lambda^2}{8\pi} \sum_{n=1}^{\infty} \frac{q_n}{1 + q_n}. \quad (17)$$

To estimate the number of modes, we utilize that radiation modes decay rapidly after a finite number of modes, similar to the estimate for spherical modes  $L \approx ka$  in (6) shown in Fig. 5. This assumption is further supported by a sum rule identity for radiation modes of homogeneous objects [27]

$$\sum_{n=1}^{\infty} q_n = \frac{2\pi\eta_0 V}{\lambda^2 \rho_r} \quad (18)$$

which demonstrates that radiation modes  $q_n$  decay, as the sum of all radiation modes is fixed and proportional to the volume and inversely proportional to the resistivity.

For typical surface resistivities of metals, such as  $R_s \approx 0.01 \Omega/\square$  for copper around 1 GHz, the radiation modes

approximately divide into two groups: those with  $q_n \gg 1$  and those with  $q_n \ll 1$  (see Fig. 5), resulting in efficiencies  $v_n$  according to

$$v_n = \frac{q_n}{1 + q_n} \approx \begin{cases} 1, & n < N_1 \\ 0, & n > N_1 \end{cases} \quad (19)$$

where  $N_1$  denotes the NDoF for the given shape and frequency. The distribution is continuous, which means that a few modes have efficiencies between 1 and 0. The transition from large to small modal efficiencies decreases with increasing electrical size (see Fig. 5).

Inserting (19) into (17) produces the estimate

$$\langle \max A_{\text{eff}} \rangle \approx \frac{\lambda^2}{8\pi} N_1. \quad (20)$$

Rewriting the partial effective area in the partial gain,  $G = 4\pi A_{\text{eff}}/\lambda^2$ , suggests that the NDoF can alternatively be expressed as

$$N_1 \approx 2 \langle \max G \rangle = \frac{1}{2} \sum \frac{q_n}{1 + q_n} \quad (21)$$

where  $\langle \max G \rangle$  denotes the average maximum partial gain [36]. This expression resembles the NDoF in [6] based on the maximal directivity in a fixed direction for a spherical region but is here generalized to arbitrarily shaped lossy objects.

The radiation modes are related to the geometrical structure by using that the maximal effective area in a direction  $\hat{\mathbf{k}}$  approaches the shadow area (geometrical cross section for convex shapes),  $A_s(\hat{\mathbf{k}})$ , in the electrically large limit [36]  $\max A_{\text{eff}}(\hat{\mathbf{k}}) \rightarrow A_s(\hat{\mathbf{k}})$  and similarly for the average over polarizations and directions

$$\langle \max A_{\text{eff}} \rangle \rightarrow \langle A_s \rangle = \frac{1}{4\pi} \int_{4\pi} A_s(\hat{\mathbf{k}}) d\Omega_{\hat{\mathbf{k}}} \quad (22)$$

as  $ka \rightarrow \infty$ . This connects the radiation modes and geometrical properties of the region  $\Omega$  with the maximal effective area (22) expressed solely in geometrical parameters producing the asymptotic NDoF

$$N_1 \approx N_A = \frac{8\pi \langle A_s \rangle}{\lambda^2} = \frac{2|A_s|}{\lambda^2} \quad \text{as } ka \rightarrow \infty \quad (23)$$

where  $|A_s| = 4\pi \langle A_s \rangle$  denotes the total shadow area. This demonstrates that the NDoF is approximately twice the total shadow area measured in squared wavelengths, where two stems from the two polarizations. Additionally, the NDoF is twice the number of significant characteristic modes [10].

The shadow area,  $A_s(\hat{\mathbf{k}})$ , is determined by illuminating the (opaque) region in the direction  $\hat{\mathbf{k}}$  and projecting the resulting shadow onto a plane perpendicular to this direction, as shown in Fig. 8. For convex shapes, the shadow area is equivalent to the maximum cross-sectional area in the given direction. Note that the shadow area is symmetric  $A_s(\hat{\mathbf{k}}) = A_s(-\hat{\mathbf{k}})$ .

The NDoF and shadow area are first analyzed for a spherical region with radius  $a$ . Due to the spherical symmetry, the shadow area is independent of the illumination direction,  $A_s(\hat{\mathbf{k}}) = \pi a^2$ , corresponding to the cross-sectional area. Consequently, the average shadow area (22) over all directions is also  $\langle A_s \rangle = \pi a^2$ . The NDoF, given by (23), is  $2(ka)^2$ ,

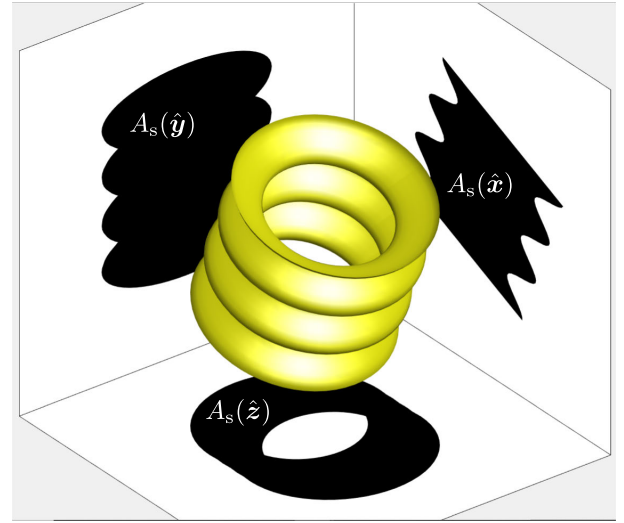


Fig. 8. Illustration of the shadow area  $A_s(\hat{\mathbf{k}})$  of a tilted corrugated cylinder for illumination directions  $\hat{\mathbf{x}}$ ,  $\hat{\mathbf{y}}$ , and  $\hat{\mathbf{z}}$ , as projected onto a plane perpendicular to each respective illumination direction.



Fig. 9. Shadow area for a region  $\Omega \in \mathbb{R}^3$ . A convex object having rays intersecting the boundary  $\partial\Omega$  twice (left). A nonconvex object with some rays intersecting the boundary more than twice (right).

consistent with the classical result in (6). The corresponding average maximal gain, derived from (21), is  $(ka)^2$ , which matches the leading term in Harrington's gain estimate [37].

For a spherical region, the total surface area,  $A = 4\pi a^2$ , is exactly four times the average shadow area,  $A = 4\langle A_s \rangle$ . This relationship is a general result for convex shapes, originally derived by Cauchy [38]

$$\langle A_s \rangle = A/4. \quad (24)$$

This identity follows from the principle that each ray intersecting the object also intersects its boundary twice [38], as illustrated in Fig. 9. For nonconvex objects, rays might intersect the boundary more than twice. This can be interpreted as shadowing of some regions, or equivalently, that some boundary points cannot radiate undestructively over  $2\pi$  steradian to the far-field. For convex objects with surface area  $A$ , the NDoF (23) reduces to

$$N_A \approx \frac{8\pi \langle A_s \rangle}{\lambda^2} \stackrel{\text{convex object}}{=} \frac{2\pi A}{\lambda^2} = \frac{k^2 A}{2\pi} \quad \text{as } ka \rightarrow \infty. \quad (25)$$

This estimate agrees with the  $L = ka$  cutoff for spherical regions (6) and Weyl's law for convex-shaped regions (5) but differ for nonconvex shapes (see Table I).

Radiation modes for six different objects are depicted in Fig. 10. The radiation mode eigenvalues  $q_n$  are normalized with the surface resistivity  $R_s$ , and the mode index  $n$  is scaled with the NDoF,  $N_A$ , based on the shadow area (23), as shown

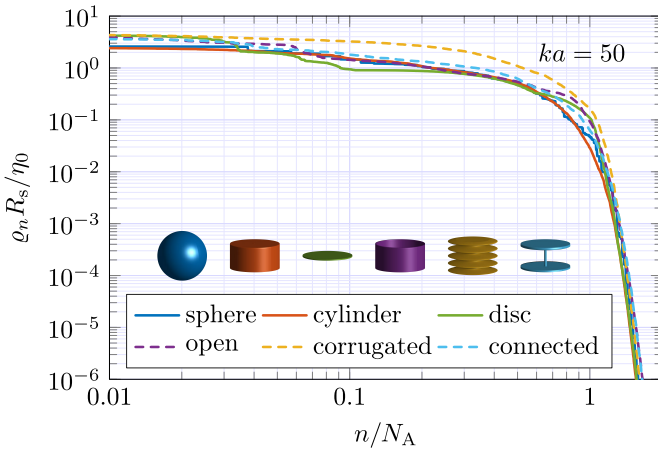


Fig. 10. Normalized radiation modes  $\varrho_n$  for the six objects in Table I of the electrical size  $ka = 50$  plotted versus the normalized mode index  $n/N_A$  (23).

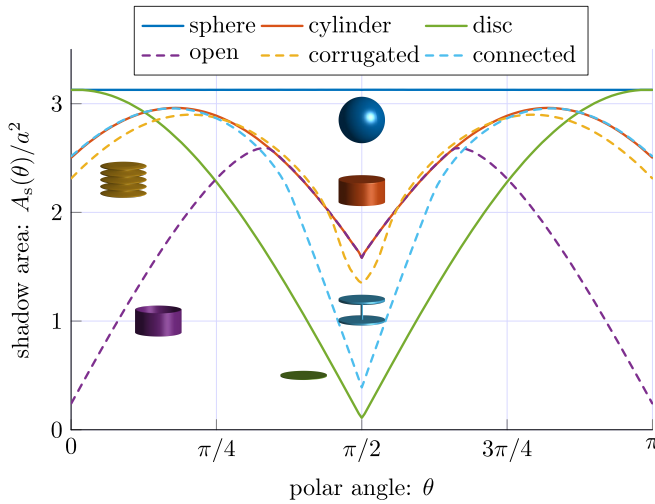


Fig. 11. Shadow areas for the six objects in Table I as a function of the polar angle  $\theta$ . The shadow areas are normalized by the smallest object's radius  $a^2$ .

in Table I. The  $N_A$  dominant normalized radiation modes have approximately unit magnitude, after which they rapidly decay.

Shadow areas for the objects in Table I are independent of the azimuthal coordinate  $\phi$  and plotted as a function of the polar angle  $\theta$  in Fig. 11. The sphere has  $A_s(\theta) = \pi a^2$  for all directions. The disk is also approximately  $A_s(0) \approx \pi a^2$  in the normal direction but much smaller seen from the side  $A_s(\theta) \approx \pi a^2 \cos \theta$ . The solid cylinder and connected disks coincide for illuminations from above,  $\theta \in [0, 0.2\pi]$ , but start to differ for illuminations from the side. The opposite holds for the cylinder compared with the open cylinder, where the opening is observed from the above but not from the side. The corrugated cylinder has a similar cross-sectional area as the cylinder but differs for illuminations from the side where the corrugations are visible (*cf.*, Fig. 8). The difference at  $\theta = 0$  is due to the different aspect ratio (see Table I). The shadow areas are bounded by  $\pi a^2$  which is reached for a sphere for all directions but also approximately for thin disks. The minimal values can approach zero, as observed for the

open cylinder at  $\theta = 0$  and disk at  $\theta = \pi/2$ . The NDoF depends on the total shadow area (23), which is determined by integration of the curves in Fig. 11 weighted by  $\sin \theta$ .

The NDoF (23) depends on the material properties such as surface resistivity  $R_s$  or bulk resistivity  $\rho_r$ . Metals typically have values  $R_s/\eta_0$  and  $k\rho_r/\eta_0$  below  $10^{-4}$  producing a distinct difference between efficient and inefficient modes as exemplified in Figs. 10 and 5. Highly resistive materials have much larger resistivity, giving fewer efficient modes and hence less DoF. Materials have here for simplicity been treated as homogeneous, but the formulation applies equally well for inhomogeneous regions.

The constraint based on material losses such as in (12) can alternatively be interpreted as restrictions of the amplitude of the current density. This is, for example, seen from the loss matrix of a homogeneous object, where the loss matrix separates into the resistance times the Gram matrix  $\mathbf{R}_\rho = \rho_r \Psi$ . Here, the least-squares norm of the current density is approximately

$$\int_{\Omega} |\mathbf{J}(\mathbf{r})|^2 dV \approx \mathbf{I}^H \Psi \mathbf{I}. \quad (26)$$

The normalized parameters  $R_s/\eta_0$  and  $k\rho_r/\eta_0$  can hence be interpreted as a weight for the current norm.

## V. ELECTRIC AND MAGNETIC CURRENTS

The NDoFs determined in Sections III and IV are based on the assumption of lossy nonmagnetic materials or similarly, a restriction on the amplitude of the electric current  $\mathbf{J}$ . However, magnetic materials and magnetic currents  $\mathbf{M}$  are also important to consider in fully understanding the NDoF of a region. Linear magnetic materials are typically lossy and can be included in the analysis using volumetric magnetic contrast currents together with a magnetic loss matrix  $\mathbf{R}_{\rho,m}$ . Magnetic surface currents are mainly important for their use as equivalent currents used to describe the field outside a region [23].

Allowing for magnetic currents increases the NDoF compared with the solely electric case. This is particularly evident for electrical sizes where the geometrical structure is not resolved by the wavelength. NDoFs of infinitely thin sheets such as planar regions do not directly follow Weyl's law, as they do not have an inner region. Considering, for example, a planar region with only electric currents enforces a symmetry of the radiated field in the up and down directions reducing the NDoF [8]. This symmetry is broken by allowing both electric and magnetic currents on the thin sheet, hence making the structure behave as a volumetric region.

Assuming magnetic losses similar to the electric loss matrix  $\mathbf{R}_\rho$  in (10) does not affect the asymptotic NDoF (23) given by the total shadow area. Numerical evaluation of the NDoF depends, however, on the loss parameters, and including magnetic currents increases NDoFs. Fig. 12 shows the radiation modes for oblate spheroids with aspect ratios  $\xi = 0.01$  and  $\xi = 0$ . The magnetic surface losses are set to correspond to the electric losses.

Consider first the case with both electric,  $\mathbf{J}$ , and magnetic currents,  $\mathbf{M}$ , shown by solid curves and markers in Fig. 12.

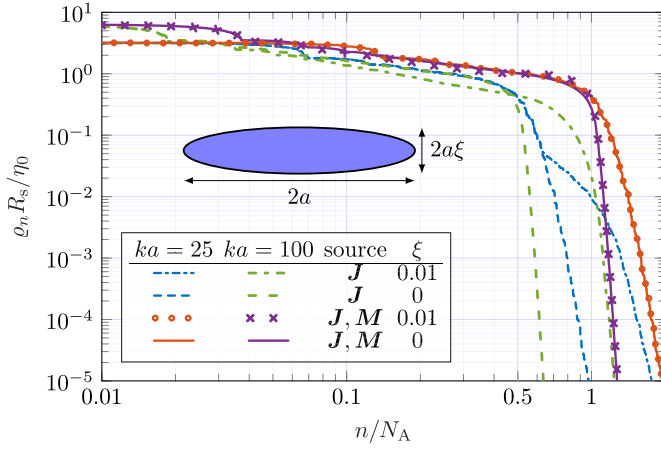


Fig. 12. Normalized radiation modes for an oblate spheroid ( $\xi = 0.01$ ) and disk ( $\xi = 0$ ) using only electric current density  $\mathbf{J}$  or both electric and magnetic  $\mathbf{M}$  current densities.

The radiation modes for oblate spheroids with  $\xi = 0.01$  and  $\xi = 0$  (infinitely thin disk) overlap. This is due to the negligible thickness of the  $\xi = 0.01$  oblate spheroid. The radiation modes  $\varrho_n$  have a cutoff around the NDoF estimate (23) based on the average shadow area  $\langle A_s \rangle = \pi a^2/2 + \pi a^2 \xi^2/(4e) \ln((1+e)/(1-e))$  with  $e^2 = 1 - \xi^2$ , which approaches  $\pi a^2/2$  as  $\xi \rightarrow 0$ . The slope of  $\varrho_n$  for  $n > N_A$  becomes steeper as  $ka$  increases, similar to the results for the sphere in Fig. 5. Here, we also note that the disk  $\xi = 0$  is treated as having a top and bottom, which is equivalent to using half the resistivity for the disk.

The purely electric case ( $\mathbf{M} = \mathbf{0}$ ) is more complex and shows a clear difference between the disk ( $\xi = 0$ ) and oblate spheroid ( $\xi = 0.01$ ). Radiation modes for the disk show a cutoff around  $n/N_A \approx 0.5$ , indicating a halving of the NDoF. This originates from the symmetric radiation of the electric currents in the disk. The finite thickness of the oblate spheroid breaks this symmetry and increases the NDoF. The radiation modes are similar up to  $n/N_A \approx 0.5$  but differ for larger mode indices  $n$ . Radiation modes for the disk decay rapidly after the cutoff around  $n/N_A \approx 0.5$  with a slope increasing with  $ka$ . Radiation modes for the oblate spheroid of the smaller size  $ka = 25$  also have a cutoff around  $n/N_A \approx 0.5$  but then deviate from the disk modes and start to approach the traces for the  $\mathbf{J}$  and  $\mathbf{M}$  cases. The  $n/N_A \approx 0.5$  cutoff vanishes for the electrically larger case  $ka = 100$ , which instead shows a  $n/N_A \approx 1$  cutoff as for the  $\mathbf{J}$  and  $\mathbf{M}$  cases. Note that the electric thickness of the oblate spheroid is  $2ka\xi \in \{0.5, 2\}$  for the  $ka \in \{25, 100\}$  cases.

Needle-shaped prolate spheroids are similarly 1-D, showing approximately a different scaling as evident from Weyl's law (4) before their thickness is resolved.

The presented derivation of the NDoFs remains valid for nonconnected and multiple objects, as demonstrated by the two square plates in Figs. 13 and 14. Fig. 13 illustrates the radiation modes  $\varrho_n$  for two plates separated by a distance  $d/\ell \in \{0.01, 0.1, 1, 10\}$ . The modal index  $n$  is normalized with the asymptotic NDoF  $N_A$  based on the average shadow area  $\langle A_s \rangle$ . Notably, the radiation modes  $\varrho_n$  exhibit a cutoff around  $N_A$ .

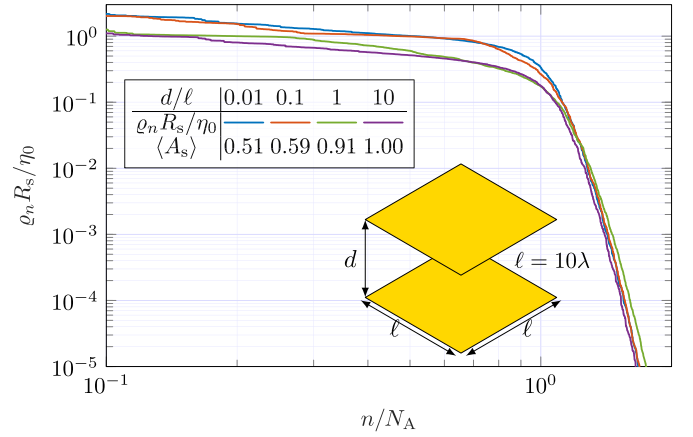


Fig. 13. Radiation modes for two square plates with side lengths  $\ell$  separated a distance  $d$  at electrical sizes  $\ell = 10\lambda$ . Electric and magnetic currents are used to emulate volumetric regions. The mode index is normalized with the asymptotic estimate (23) based on the average shadow area  $\langle A_s \rangle$ .

The shadow area can be numerically evaluated by considering the projected area of the two squares in a plane parallel to the plates. This resulting shadow area, plotted versus the distance  $d$ , is illustrated in Fig. 14 by the curve  $\langle A_s(d/\ell) \rangle / \langle A_s(0) \rangle$ , where  $\langle A_s(0) \rangle = \ell^2/2$  represents the average shadow area for a single square, as shown in (24). As the distance increases, the average shadow area also increases and approaches  $2\langle A_s(0) \rangle$  as  $d/\ell \rightarrow \infty$ , corresponding to the NDoF of a plate with an area of  $2\ell^2$ .

The effective NDoFs (13) for  $\ell/\lambda \in \{10, 20\}$  are depicted in Fig. 14. The curves align with the trend of the asymptotic value (23) derived from the average shadow area  $\langle A_s \rangle(d/\ell)$ . Moreover, they converge toward the asymptotic result as the electrical size increases, as observed for the  $\ell/\lambda \in \{10, 20\}$  cases.

## VI. INVERSE SOURCE PROBLEM

The concept of NDoFs for radiating systems, as analyzed in Section IV, also applies to inverse source problems. Consider a region composed of some linear material. By employing the equivalence principle, the radiated field can be represented by electric  $\mathbf{J}$  and magnetic  $\mathbf{M}$  surface current densities on a surface  $\Omega$  surrounding the region [39]. For simplicity, we let this surface coincide with the boundary  $\Omega$  of the region. With all sources inside  $\Omega$ , Love's theorem or the null field condition can be used to relate the electric and magnetic currents in the inverse source problem [40], [41].

Considering for simplicity electrical currents on a PEC object (see Fig. 15). Expanding the measured field in spherical waves with expansion coefficients  $f_n$  and adding noise to the measured field (expansion coefficients). This results in the measurement model

$$\mathbf{f} = -\mathbf{U}\mathbf{I} + \mathbf{n} \quad (27)$$

which resembles the communication model in Section III. In inverse source problems, the source current  $\mathbf{I}$  is estimated from the observed field  $\mathbf{f}$ . The system (27) is not invertible,



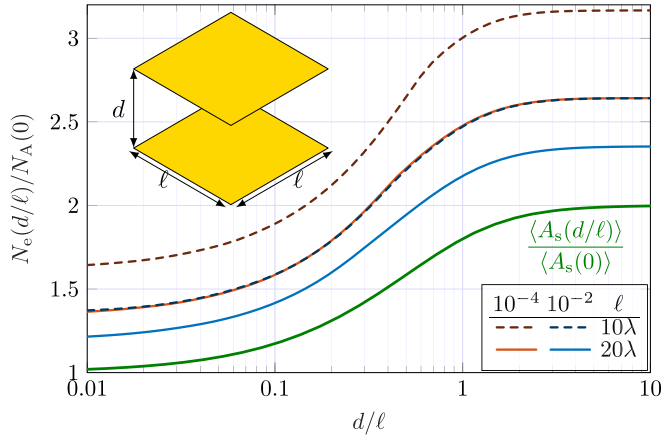


Fig. 14. Effective DoF (13) for two square plates with side lengths  $\ell$  separated a distance  $d$  at electrical sizes  $\ell/\lambda \in [10, 20]$ . Electric and magnetic currents are used to emulate volumetric regions. The eNDoF is normalized with the asymptotic estimate (23) evaluated for a single plate. The results are compared with the average shadow area for distances  $d/\ell$  normalized with the average shadow area for a single plate.

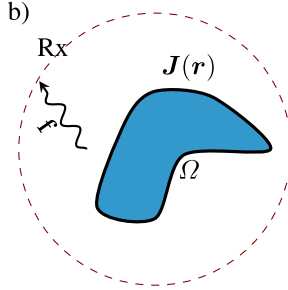


Fig. 15. Inverse source problem for a region with surface  $\Omega$  with measurements in the far-field or on a circumscribing sphere.

and it is common to reformulate the system as an optimization problem or to use an SVD for a regularized solution [42].

Regularizing the inverse source problem (27) by penalizing the norm of the current density [42], for example,

$$\begin{aligned} \min_{\mathbf{I}} \|\mathbf{U}\mathbf{I} + \mathbf{f}\|^2 + \delta\eta_0 \|\mathbf{I}\|_{\Omega}^2 \\ = \min_{\mathbf{I}} \mathbf{I}^H \mathbf{R}_\rho \mathbf{I} + 2 \operatorname{Re}\{\mathbf{f}^H \mathbf{U}\mathbf{I}\} + |\mathbf{f}|^2 + \delta\eta_0 \mathbf{I}^H \Psi \mathbf{I} \end{aligned} \quad (28)$$

where the induced metric (26) from  $\Omega$  is used for the current. Here, the regularization term  $\delta\eta_0 \mathbf{I}^H \Psi \mathbf{I}$  has the same form as for the dissipated power in the material from the material matrix  $\mathbf{R}_\rho$  in (9), that is, the regularization parameter  $\delta$  mimics the normalized surface resistivity  $R_s/\eta_0$ . This similarity reveals a connection between the physical bounds formulated in currents [30] and inverse source problems.

Expanding the current

$$\mathbf{I} = \sum_n I_n \mathbf{I}_n \quad (29)$$

in radiation modes (11) defined by using  $\mathbf{R}_\rho = \eta_0 \Psi$  to diagonalize (28)

$$\min_{I_n} \sum_n (\varrho_n + \delta) |I_n|^2 + 2 \operatorname{Re}\{f_n^* I_n \sqrt{\varrho_n}\} + |f_n|^2 \quad (30)$$

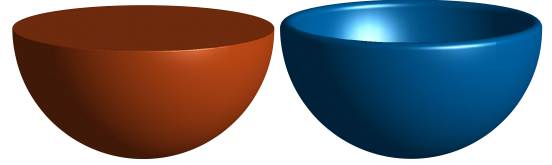


Fig. 16. Inverse source problems for a hemisphere (convex) and a bowl (nonconvex). Both objects have radius  $a$ .

with the solution

$$I_n = -\frac{\sqrt{\varrho_n}}{\delta + \varrho_n} f_n. \quad (31)$$

The corresponding solution using an SVD is

$$I_n = -f_n / \sqrt{\varrho_n}. \quad (32)$$

The solutions (32) and (31) are similar for efficient radiation modes  $\varrho_n \gg 1$  but differ for inefficient modes  $\varrho_n \ll 1$ . Inefficient radiation modes make the noise in (27) blow up for (32) unless they are removed in the pseudo-inverse related to the SVD. The (Tikhonov) regularized solution has a smoother transition where the impact of inefficient modes decreases as  $\sqrt{\varrho_n}$ . The efficient modes are also the ones contributing to the NDoF.

These simple problems demonstrate the utility of NDoF derived from radiation modes and, asymptotically, from the shadow area in understanding inverse source problems. Employing the asymptotic NDoF offers a straightforward estimation of resolution in such problems. For instance, if the surface area is  $|\Omega|$ , then there are approximately  $2\pi|\Omega|/\lambda^2$  DoF for the current density on  $\Omega$  according to (5), while the measured data contributes approximately  $8\pi\langle A_s \rangle/\lambda^2$  DoF based on the average shadow area  $\langle A_s \rangle$ .

As an example, consider a hemisphere (half ball) with radius  $a$  and a half-spherical shell with radius  $a$  and thickness  $a/10$ , as depicted in Fig. 16. The hemisphere is convex and has a surface area  $A = 3\pi a^2$  and an average shadow area  $\langle A_s \rangle = A/4 = 3\pi a^2/4$ . The half-spherical shell has an identical shadow area and an approximate surface area  $A \approx 4\pi a^2$  (assuming thin walls). This implies that the radiating NDoF asymptotically is the same for the two objects, but the nonconvex bowl has a larger surface area over which the current is reconstructed. This suggests that the same NDoF is used to reconstruct the current density over different surface areas. As a consequence, this reduces the (average) resolution from approximately  $\lambda/1.8$  for the hemisphere with 75% to approximately  $\lambda/1.5$  for the bowl.

## VII. CONCLUSION

We present a method for determining the NDoF for a radiating system based on radiation modes. Asymptotically, the NDoF approaches the total shadow area measured in squared wavelengths. For convex regions, the NDoF matches the results derived from Weyl's law. The findings extend the known expressions to arbitrary shapes, encompassing nonconvex and nonconnected regions. Numerical results complementing the theoretical framework and comparing them with the shadow area are provided. The derivation of the NDoF

is linked to upper limits on the capacity (spectral efficiency) for a communication channel between an object and the far-field, as well as to inverse source problems with measurements surrounding an object.

#### APPENDIX A RADIATION MODES

Radiation modes for spherical geometries are determined by expanding the field in spherical waves parametrized by  $\tau \in \{1, 2\}$  and  $l \geq 1$  and ordered by an index  $n$  [24]. Homogeneous spherical (ball) regions with resistivity  $\rho_\tau$  and radius  $a$  are expressed as [27]

$$\varrho_n = \frac{k^2 a^3 \eta_0}{2\rho_\tau} \left( \left( R_{1,l}^{(1)} \right)^2 - R_{1,l-1}^{(1)} R_{1,l+1}^{(1)} + \frac{2}{ka} R_{1,l}^{(1)} R_{2,l}^{(1)} \delta_{\tau,2} \right) \quad (33)$$

and for a spherical shell with surface resistivity  $R_s$  as

$$\varrho_n = \frac{k^2 a^2 \eta_0}{R_s} \left( R_{\tau,l}^{(1)} \right)^2 \quad (34)$$

where  $R_{\tau,l}$  denotes radial functions [24] evaluated for  $ka$ ,  $\delta_{1,2} = 0$ , and  $\delta_{2,2} = 1$ .

#### APPENDIX B DIRECTIONAL AND POLARIZATION AVERAGES

Expressing the solution (15) in spherical waves with expansion coefficients collected in a column matrix  $\mathbf{a}$  using  $\mathbf{F} = \mathbf{U}^T \mathbf{a} / (4\pi)$  [27] yields

$$\max A_{\text{eff}} = \lambda^2 \mathbf{F}^H \mathbf{R}^{-1} \mathbf{F} = \frac{\lambda^2}{16\pi^2} \mathbf{a}^H \mathbf{U} \mathbf{R}^{-1} \mathbf{U}^T \mathbf{a}. \quad (35)$$

Diagonalizing (35) using radiation modes (11) induces a change of variables  $\tilde{\mathbf{a}} = \mathbf{Q} \mathbf{a}$  with a unitary matrix  $\mathbf{Q}$  having elements  $Q_{nm}$

$$\max A_{\text{eff}} = \frac{\lambda^2}{16\pi^2} \sum_n \frac{\varrho_n |\tilde{a}_n|^2}{1 + \varrho_n} = \frac{\lambda^2}{16\pi^2} \sum_{n,m} \frac{\varrho_n Q_{nm}^2 |a_m|^2}{1 + \varrho_n} \quad (36)$$

where  $\sum_m Q_{nm}^2 = 1$ . Taking the average (16) of  $\max A_{\text{eff}}$  and using the plane wave expansion  $a_n = 4\pi j^{\tau-1-l} \hat{\mathbf{e}} \cdot \mathbf{Y}_n(\hat{\mathbf{k}})$  [23] with spherical harmonics  $\mathbf{Y}_n$  and  $\hat{\mathbf{e}} \cdot \hat{\mathbf{k}} = 0$  results in

$$\begin{aligned} \langle |a_n|^2 \rangle &= \frac{1}{8\pi^2} \int_{2\pi} \int_{4\pi} |a_n|^2 d\Omega_{\hat{\mathbf{k}}} d\Omega_{\hat{\mathbf{e}}} \\ &= 2 \int_{4\pi} \mathbf{Y}_v(\hat{\mathbf{k}}) \cdot \int_{2\pi} \hat{\mathbf{e}} \hat{\mathbf{e}} d\Omega_{\hat{\mathbf{e}}} \cdot \mathbf{Y}_v(\hat{\mathbf{k}}) d\Omega_{\hat{\mathbf{k}}} \\ &= 2\pi \int_{4\pi} \mathbf{Y}_v(\hat{\mathbf{k}}) \cdot \mathbf{Y}_v(\hat{\mathbf{k}}) d\Omega_{\hat{\mathbf{k}}} = 2\pi \end{aligned} \quad (37)$$

where the middle integral is, without loss of generality, evaluated for an arbitrarily fixed direction  $\hat{\mathbf{e}} = \hat{\mathbf{z}}$  as

$$\int_{2\pi} \hat{\mathbf{e}} \hat{\mathbf{e}} d\Omega_{\hat{\mathbf{e}}} = \int_{2\pi} \hat{\mathbf{x}} \hat{\mathbf{x}} \cos^2 \theta + \hat{\mathbf{y}} \hat{\mathbf{y}} \sin^2 \theta d\theta = \pi (\hat{\mathbf{x}} \hat{\mathbf{x}} + \hat{\mathbf{y}} \hat{\mathbf{y}}) \quad (38)$$

and using that  $\hat{\mathbf{k}} \cdot \mathbf{Y}(\hat{\mathbf{k}}) = 0$  extends (38) to an identity dyadic. The same relation (37) holds for the orthogonal combination  $\langle |\tilde{a}_n|^2 \rangle = \sum Q_{mn}^2 \langle |a_n|^2 \rangle = 2\pi$  giving the simple identity (17) for the average maximal effective area expressed in radiation modes.

#### REFERENCES

- [1] O. M. Bucci and G. Franceschetti, "On the degrees of freedom of scattered fields," *IEEE Trans. Antennas Propag.*, vol. 37, no. 7, pp. 918–926, Jul. 1989.
- [2] O. M. Bucci and T. Isernia, "Electromagnetic inverse scattering: Retrievable information and measurement strategies," *Radio Sci.*, vol. 32, no. 6, pp. 2123–2137, Nov. 1997.
- [3] R. Piestun and D. A. B. Miller, "Electromagnetic degrees of freedom of an optical system," *J. Opt. Soc. Amer. A, Opt. Image Sci.*, vol. 17, no. 5, pp. 892–902, 2000.
- [4] M. D. Migliore, "On the role of the number of degrees of freedom of the field in MIMO channels," *IEEE Trans. Antennas Propag.*, vol. 54, no. 2, pp. 620–628, Feb. 2006.
- [5] M. D. Migliore, "On electromagnetics and information theory," *IEEE Trans. Antennas Propag.*, vol. 56, no. 10, pp. 3188–3200, Oct. 2008.
- [6] P.-S. Kildal, E. Martini, and S. Maci, "Degrees of freedom and maximum directivity of antennas: A bound on maximum directivity of nonsuperreactive antennas," *IEEE Antennas Propag. Mag.*, vol. 59, no. 4, pp. 16–25, Aug. 2017.
- [7] S. Hu, F. Rusek, and O. Edfors, "Beyond massive MIMO: The potential of data transmission with large intelligent surfaces," *IEEE Trans. Signal Process.*, vol. 66, no. 10, pp. 2746–2758, May 2018.
- [8] C. Ehrenborg and M. Gustafsson, "Physical bounds and radiation modes for MIMO antennas," *IEEE Trans. Antennas Propag.*, vol. 68, no. 6, pp. 4302–4311, Jun. 2020.
- [9] A. Pizzo, A. D. J. Torres, L. Sanguinetti, and T. L. Marzetta, "Nyquist sampling and degrees of freedom of electromagnetic fields," *IEEE Trans. Signal Process.*, vol. 70, pp. 3935–3947, 2022.
- [10] M. Gustafsson and J. Lundgren, "Degrees of freedom and characteristic modes," *IEEE Antennas Propag. Mag.*, vol. 66, no. 6, pp. 18–28, Dec. 2024.
- [11] D. A. B. Miller, "Waves, modes, communications, and optics: A tutorial," *Adv. Opt. Photon.*, vol. 11, no. 3, pp. 679–825, 2019.
- [12] G. T. Di Francia, "Resolving power and information," *J. Opt. Soc. Amer.*, vol. 45, no. 7, p. 497, Jul. 1955.
- [13] G. Di Francia, "Directivity, super-gain and information," *IRE Trans. Antennas Propag.*, vol. 4, no. 3, pp. 473–478, Jul. 1956.
- [14] D. A. Hill, "Electronic mode stirring for reverberation chambers," *IEEE Trans. Electromagn. Compat.*, vol. 36, no. 4, pp. 294–299, Nov. 1994.
- [15] H. Weyl, "Über die asymptotische verteilung der eigenwerte," *Nachrichten von der Gesellschaft der Wissenschaften zu Göttingen, Mathematisch-Physikalische Klasse*, vol. 1911, pp. 110–117, Jan. 1911.
- [16] W. Arendt, R. Nittka, W. Peter, and F. Steiner, "Weyl's law: Spectral properties of the Laplacian in mathematics and physics," in *Mathematical Analysis of Evolution, Information, and Complexity*. Hoboken, NJ, USA: Wiley, 2009, pp. 1–71.
- [17] O. M. Bucci, C. Gennarelli, and C. Savarese, "Representation of electromagnetic fields over arbitrary surfaces by a finite and nonredundant number of samples," *IEEE Trans. Antennas Propag.*, vol. 46, no. 3, pp. 351–359, Mar. 1998.
- [18] M. Franceschetti, *Wave Theory of Information*. Cambridge, U.K.: Cambridge Univ. Press, 2017.
- [19] P. Hannan, "The element-gain paradox for a phased-array antenna," *IEEE Trans. Antennas Propag.*, vol. AP-12, no. 4, pp. 423–433, Jul. 1964.
- [20] P.-S. Kildal, A. Vosoogh, and S. Maci, "Fundamental directivity limitations of dense array antennas: A numerical study using Hannan's embedded element efficiency," *IEEE Antennas Wireless Propag. Lett.*, vol. 15, pp. 766–769, 2016.
- [21] M. Gustafsson, "Shadow area and degrees of freedom for free-space communication," 2024, *arXiv:2407.21122*.
- [22] R. F. Harrington, *Time Harmonic Electromagnetic Fields*. New York, NY, USA: McGraw-Hill, 1961.
- [23] G. Kristensson, *Scattering of Electromagnetic Waves By Obstacles*. Edison, NJ, USA: SciTech Publishing, 2016.
- [24] J. E. Hansen, Ed., *Spherical Near-Field Antenna Measurements* (IEE Electromagnetic Waves Series), no. 26. Stevenage, U.K.: Peter Peregrinus Ltd., 1988.
- [25] J. Song and W. C. Chew, "Error analysis for the truncation of multipole expansion of vector Green's functions [EM scattering]," *IEEE Microw. Wireless Compon. Lett.*, vol. 11, no. 7, pp. 311–313, Jul. 2001.
- [26] K. R. Schab, "Modal analysis of radiation and energy storage mechanisms on conducting scatterers," Ph.D. dissertation, Dept. Elect. Comput. Eng., Univ. Illinois at Urbana-Champaign, 2016.

- [27] M. Gustafsson, K. Schab, L. Jelínek, and M. Čapek, "Upper bounds on absorption and scattering," *New J. Phys.*, vol. 22, no. 7, Mar. 2020, Art. no. 073013.
- [28] M. A. Jensen and J. W. Wallace, "Capacity of the continuous-space electromagnetic channel," *IEEE Trans. Antennas Propag.*, vol. 56, no. 2, pp. 524–531, Feb. 2008.
- [29] R. F. Harrington, *Field Computation by Moment Methods*. New York, NY, USA: Macmillan, 1968.
- [30] M. Gustafsson and S. Nordebo, "Optimal antenna currents for Q, superdirectivity, and radiation patterns using convex optimization," *IEEE Trans. Antennas Propag.*, vol. 61, no. 3, pp. 1109–1118, Mar. 2013.
- [31] C. Ehrenborg and M. Gustafsson, "Fundamental bounds on MIMO antennas," *IEEE Antennas Wireless Propag. Lett.*, vol. 17, pp. 21–24, 2018.
- [32] C. Ehrenborg, M. Gustafsson, and M. Capek, "Capacity bounds and degrees of freedom for MIMO antennas constrained by Q-factor," *IEEE Trans. Antennas Propag.*, vol. 69, no. 9, pp. 5388–5400, Sep. 2021.
- [33] A. Paulraj, R. Nabar, and D. Gore, *Introduction to Space-Time Wireless Communications*. Cambridge, U.K.: Cambridge Univ. Press, 2003.
- [34] D. S. Shiu, G. J. Foschini, M. J. Gans, and J. M. Kahn, "Fading correlation and its effect on the capacity of multielement antenna systems," *IEEE Trans. Commun.*, vol. 48, no. 3, pp. 502–513, Mar. 2000.
- [35] S. S. A. Yuan, Z. He, X. Chen, C. Huang, and W. E. I. Sha, "Electromagnetic effective degree of freedom of an MIMO system in free space," *IEEE Antennas Wireless Propag. Lett.*, vol. 21, no. 3, pp. 446–450, Mar. 2022.
- [36] M. Gustafsson and M. Capek, "Maximum gain, effective area, and directivity," *IEEE Trans. Antennas Propag.*, vol. 67, no. 8, pp. 5282–5293, Aug. 2019.
- [37] R. F. Harrington, "Effect of antenna size on gain, bandwidth, and efficiency," *J. Res. Nat. Bur. Standards D. Radio Propag.*, vol. 64D, no. 1, pp. 1–12, Jan. 1960.
- [38] V. Vouk, "Projected area of convex bodies," *Nature*, vol. 162, no. 4113, pp. 330–331, Aug. 1948.
- [39] J. G. van Bladel, *Electromagnetic Fields*, 2nd ed., Piscataway, NJ, USA: IEEE Press, 2007.
- [40] K. Persson and M. Gustafsson, "Reconstruction of equivalent currents using a near-field data transformation—With radome applications," *Prog. Electromagn. Res.*, vol. 54, pp. 179–198, 2005.
- [41] J. L. A. Quijano and G. Vecchi, "Field and source equivalence in source reconstruction on 3D surfaces," *Prog. Electromagn. Res.*, vol. 103, pp. 67–100, 2010.
- [42] P. C. Hansen, *Discrete Inverse Problems: Insight and Algorithms*, vol. 7. Philadelphia, PA, USA: Society for Industrial & Applied Mathematics, 2010.



**Mats Gustafsson** (Senior Member, IEEE) received the M.Sc. degree in engineering physics and the Ph.D. degree in electromagnetic theory from Lund University, Lund, Sweden, 1994 and 2000, respectively.

He was appointed as a Docent in 2005 and a Professor of Electromagnetic Theory with Lund University in 2011. He co-founded the company Phase Holographic Imaging AB, Lund, in 2004. He has written over 100 peer-reviewed journal articles and over 100 conference papers. His research interests are in scattering and antenna theory and inverse scattering and imaging.

Prof. Gustafsson received the IEEE Schelkunoff Transactions Prize Paper Award 2010, the IEEE Uslenghi Letters Prize Paper Award 2019, and the Best Paper Awards at EuCAP 2007 and 2013. He served as an IEEE AP-S Distinguished Lecturer from 2013 to 2015.